Hindawi
Security and Communication Networks
Volume 2022, Article ID 9797309, 1 page
https://doi.org/10.1155/2022/9797309

Retraction

Retracted: Prediction Model for Driver Reaction Time Based on PSO-BP Neural Network Model

Security and Communication Networks

Received 16 November 2022; Accepted 16 November 2022; Published 7 December 2022

Security and Communication Networks has retracted the article titled "Prediction Model for Driver Reaction Time Based on PSO-BP Neural Network Model" [1] due to concerns that the peer review process has been compromised.

Following an investigation conducted by the Hindawi Research Integrity team [2], significant concerns were identified with the peer reviewers assigned to this article; the investigation has concluded that the peer review process was compromised. We therefore can no longer trust the peer review process, and the article is being retracted with the agreement of the Chief Editor.

References

[1] D. Wang, H. Liang, C. Zhang, Y. Bai, Z. Z. Bi, and Y. Lin, "Prediction Model for Driver Reaction Time Based on PSO-BP Neural Network Model," *Security and Communication Networks*, vol. 2022, Article ID 6100702, 13 pages, 2022.

[2] L. Ferguson, "Advancing Research Integrity Collaboratively and with Vigour," 2022, https://www.hindawi.com/post/advancing-research-integrity-collaboratively-and-vigour/.

Hindawi
Security and Communication Networks
Volume 2022, Article ID 6100702, 13 pages
https://doi.org/10.1155/2022/6100702

Research Article

Prediction Model for Driver Reaction Time Based on PSO-BP Neural Network Model

Dan Wang, Liang Hong, Ce Zhang, Yajie Bai, Zhen Zhen Bi, and Yier Lin

School of Mechanical Engineering, Tianjin University of Science and Technology, Tianjin, China

Correspondence should be addressed to Yier Lin; yier.lin@tust.edu.cn

Received 13 June 2022; Revised 5 July 2022; Accepted 12 July 2022; Published 10 August 2022

Academic Editor: Mohammad Ayoub Khan

A critical element of accident reconstruction technology is the driver reaction time, which is also a key aspect of evaluating driver takeover time in autonomous driving. There are various factors affecting driver reaction time, including driver psychological factors, nondriving tasks, external environment, and other reasons. It is necessary to record and predict the driver reaction time to support the takeover time in the degraded takeover study because this paper is designed to conduct a degraded takeover study in the human-machine codriving stage with safety of the intended functionality. Therefore, a model based on PSO-BP neural network algorithm to predict driver reaction time is developed. A wavelet transform algorithm is used to denoise the signal first in order to improve the convergence speed and prediction accuracy of the model. Meanwhile, the BP neural network prediction model based on the PSO is established to optimize the weights and thresholds of the BP neural network to achieve the prediction of the driver reaction time. A total of six main feature parameters of driver's HRV in the time and frequency domains were selected as input indicators and substituted into the input signal of PSO-BP neural network model for training and testing. The prediction results obtained from the PSO-BP neural network model were compared with that of the BP neural network prediction, and it demonstrated that the prediction results obtained in this paper have smaller error values, verifying the reasonableness and validity of the model.

1. Introduction

There are three segments of autonomous vehicle safety: functional safety, safety of the intended functionality (SOTIF), and information security. As a result of the complexity and unknowns of the operating conditions of autonomous vehicles, there may be a considerable risk of safe operation even if the autonomous driving function fulfils the design requirements. SOTIF is defined as no unreasonable risk due to hazards caused by inadequate design or performance limitations. In other words, the risks caused by design deficiencies and performance limitations are controlled within a reasonable and acceptable margin. These design deficiencies and performance limitations will lead to whole vehicle operational hazards when specific scenario triggering conditions are encountered, such as environmental interference or human misuse. A critical part of the *L*0 to *L*3 system is switching to a human driver in the occurrence of a failure. Much research is required to switch from an autonomous driving system to a human driver. It takes anywhere from 2 to 26 seconds to complete the switch in a nonemergency situation. When the switch request is received, it takes longer if the driver is engaged in other tasks. Drivers are more likely to react slowly in emergencies. Meanwhile, drivers may make inappropriate decisions and cause accidents. The proportion of accidents caused by inattentiveness of drivers is already at a very high level. Furthermore, it is less likely that such a driver is well prepared to take over the vehicle in an emergency. Therefore, the problem of driver takeover time during the autonomous driving control switch needs to be studied. Moreover, the takeover time will contain the driver reaction time. It is crucial to consider the driver reaction time under different nondriving tasks and the reaction time under unexpected events.

The driver's reaction time is split into pure and selective reactions. Pure reaction time refers to a single stimulus signal, which means that the driver only reacts to one stimulus signal, and the time is recorded. Selective reaction time refers to the complex stimulus signal, which requires the driver to judge different stimulus signals and react accordingly. As the paper is designed for the human-machine codriving phase to perform the degradation of SOTIF to take over the research, thus, it is necessary to record and predict the simple reaction time of the driver to provide data to support the takeover time in the degraded takeover study. Therefore, this paper selects a single stimulus signal to test the driver's reaction time. The studies on driver reaction times are currently based on indoor experiments and driving simulators to estimate reaction times [1]. The so-called reflex devices are used in testing reaction time situations. Time for a reaction is evaluated as the time from the occurrence of a given light or sound stimulus signal to pressing an appropriate button on the table. The data are tracked experimentally on the road or during the test. Generally, the test results of these responses are so-called simple stimuli signal (single light or sound signal), while the driver's response is also simplified—it should act on a car control factor (stepping on the brake pedal, operating the hand brake lever, or steering wheel) [2]. Drodziel et al. described the findings of a study of total driver reaction time in real traffic conditions. The tested drivers had to respond to complex signals by performing braking operations. There were 15 drivers with different driving license qualifications in the study team. Both perception and leg shift times were measured from the gas pedal to the brake pedal. An absence of correlation between driving seniority and total reaction time was found [3]. Johansson and Rumar studied braking reaction time in 321 subjects and found that the estimated reaction time varied from 0.4 to 2.7 s with a mean and standard deviation of 1.01 and 0.37 s. Given that the drivers were told they were participating in a braking response study and a sound would be used as a stimulus signal, these values may be biased [4]. Durrani et al. studied to determine the perception-reaction time (PRT) for different spacing under approach and braking conditions. Meanwhile, they examined the relationship between PRT and deceleration rate with crash risk. There were three hypotheses of PRT tested, including perception and response thresholds and an evidence accumulation framework using visual variables (tau-inverse). It was shown that an evidence accumulation framework is a promising approach to predicting driver responses under different types of guided vehicle approaches and braking conditions. Moreover, there is an important urgency in predicting crash probability [5]. Jurecki, Rafał described the average values of driver response times in TTC functions obtained in six different scenarios. A linear regression equation for determining the average response time was involved in these studies. It was shown that the value of the response time depends strongly on the type of emergency and the value of the TTC. It is suggested that the value of response time can be used to reconstruct computer-based road accidents [6]. The data collected from two controlled field experiments on Virginia Tech Transportation Institute (VTTI) smart roads were used by Elhenawy et al. to simulate the braking PRT and the level of deceleration at the onset of the yellow indication for different road conditions. Many of the latest machine-learning techniques are used in the paper to train the models. These models can predict the braking perceived reaction time PRT and deceleration level close to the driver [7]. Two different studies were performed by Poliak, Milos, et al. on the simulator with 120 participants (professional drivers). The first experiment involved 116 drivers. The second experiment was done with four drivers. The experiment used eye-tracking technology. Statistical tests were used to determine the mean reaction time. Statistical tests, regression models, and clustering were used to assess the effect of age on the reaction time of professional drivers [8]. Nowosielski et al. evaluated the effect of mental workload on reaction time by studying the differences in reaction times of drivers in different age groups. The experiment was performed in simulated streets and other conditions to identify drivers with relatively longer reaction times and those whose reaction times were significantly influenced by mental workload when driving on public roads. The reaction time after hearing the buzzer was measured in five conditions: (1) sit in a stationary vehicle; (2) perform mental calculations in a stationary vehicle; (3) drive on a simulated street; (4) perform mental calculations while driving on a simulated street; (5) drive on a public road. There were other differences between age groups and individuals for the mental calculations and other differences in individual performance for each driver. Mental calculations increased differences among age groups and individuals, and increased differences in respective drivers' individual performance. [9]. An efficient advanced driver assistance system (ADAS) is expected to provide safety alerts before the driver becomes aware of the potential for rear-end collisions to reduce response times to prevent collisions. Therefore, the use of individualized response times can significantly improve the safety performance of ADAS compared to using average values for all drivers and driving conditions. Arbabzadeh developed a statistical model to estimate the brake-stop response time in a rear-end conflict scenario. Both intrinsic driver characteristics and other additional background variables were factored into the model [10]. A study of driver behaviour in a simulated precrash situation is discussed by Jurecki et al. The tests were conducted on a race track to determine the driver's reaction time to a pedestrian approaching from the left or right side. It used a specially developed test stand with a pedestrian model. The analysis involved the determination of linear regression equations with mean, standard deviation, and 0.1, 0.25, 0.75, and 0.9 quartiles [11].

This paper performs a driver reaction time testing study for the SOTIF triggering scenario. A model for predicting driver reaction time in the SOTIF triggering scenario is built. The physiological electrocardiogram (ECG) signal of the driver is considered the driver reaction time-related index in this paper. The driver ECG signal is obtained by building a driving simulator, physiological instrument, and other bench tests. Meanwhile, the data are preprocessed. Pearson correlation analysis selects the feature parameters for predicting the

driver reaction time model to construct the PSO (particle swarm optimization)-BP neural network prediction model. Finally, the prediction of driver reaction time is obtained. As far as we know, this paper is the first study of driver reaction time prediction based on the SOTIF trigger scenario. The PSO algorithm finds the optimal weights and thresholds of the BP neural network to establish the PSO-BP neural network prediction model. The remainder of this paper is organized as follows. We developed a new wavelet transform-based denoising in Section 2. The relevant model principles and algorithmic procedures are described based on the PSO-BP neural network prediction model. We introduced the experimental setup and the analysis and processing of the data in Section 3. In Section 4, the experimental results are presented. In Section 5, a conclusion of this paper is given.

2. Theoretical Approach

2.1. Algorithm Process. A simulated automated vehicle platform was built using PRESCAN driving simulator. A wavelet transform is used to denoise the obtained signals. The RR intervals are obtained by locating the *R* waves in the QRS wave group of the ECG signal and then extracting the heart rate variability (HRV) parameters in the time domain and frequency domain. The prediction model of the PSO-BP neural network is constructed with the driver ECG parameters as the input layer and the reaction time as the output layer. The number of particle populations in this paper is 10, and the dimension of one particle is 57. The root mean square error (RMSE) is selected as the adaptability function of PSO. The optimal solution is iteratively substituted into the BP neural network for training and testing. The flow chart of the algorithm is shown in Figure 1.

2.2. Selection of Characteristic Parameters of ECG Signal Based on Wavelet Transform. The ECG signal is used as a predictor of driver reaction time in this paper to predict driver reaction time objectively, accurately, cost-effectively, and without interference. The noise interference in the ECG signal reduces the signal-to-noise ratio of the ECG signal. It affects the subsequent processing and detection of the signal because there are various noise interferences in the ECG signal extraction process, such as industrial frequency interference, myoelectric interference, and baseline drift. A wavelet transform algorithm is first used to denoise the original data to remove the noisy signal. Then, the HRV is extracted from the denoised signal. The RR interval is determined by eliminating the R-peak position of the QRS waveform from the ECG signal. Then, the HRV is extracted from the time domain and frequency domain as the input parameters of the PSO-BP neural network model.

HRV refers to the minor differences in time between consecutive regular cardiac cycles. It is known from the literature that the RR interval represents the spacing between adjacent QRS wave groups. The reflection of the ventricular rate is done by subtracting the sampling time of the previous peak from the sampling time of the last peak. The time-domain parameters of the HRV signal are defined as follows.

The NNVGR represents the mean of the total normal sinus interval (RR) in ms, which is

$$\mathrm{NNVGR} = \frac{1}{N}\sum_{i=1}^{N} \mathrm{RR}. \tag{1}$$

SDNN: standard deviation of normal to normal represents the standard deviation of the full RR interval in ms, which is

$$\mathrm{SDNN} = \sqrt{\frac{1}{N}\sum_{i=1}^{N-1}\left(\mathrm{RR}_i - \overline{\mathrm{RR}}\right)^2}. \tag{2}$$

RMSSD: it represents the root mean square of the difference of successive RR interval differences throughout, which is

$$\mathrm{RMSSD} = \sqrt{\frac{1}{N-1}\sum_{i=1}^{N-1}\left(\mathrm{RR}_{i-1} - \mathrm{RR}_i\right)^2}. \tag{3}$$

SDSD represents the standard deviation of the difference between the lengths of adjacent RR intervals throughout in ms, which is

$$\mathrm{SDSD} = \sqrt{\frac{1}{N-1}\sum_{i=1}^{N-1}\left(\mathrm{RR}'_i - \overline{\mathrm{RR}'}\right)^2}, \tag{4}$$

where $\mathrm{RR}'_i = \mathrm{RR}_i - \mathrm{RR}_{i+1}$, $\overline{\mathrm{RR}\prime} = (\overline{\mathrm{RR}} - \mathrm{RR}_{i+1})^2$.

NN50: number of pairs of adjacent RR intervals differing by more than 50 ms in the entire recording.

pNN50: percentage of successive RR intervals that differ by more than 50 ms %, which is

$$p\mathrm{NN50} = \frac{\mathrm{NN50}}{num_{NN}}. \tag{5}$$

The frequency domain of the HRV signal includes TP (total power), HF (high-frequency power), LF (low-frequency power), and LF/HF (ratio of LF-to-HF power). Where the unit of TP is ms^2, which represents the sum of high frequency, low frequency, and very low frequency of all normal interbeat interval variants. HF refers to the high-frequency range of power (0.15 Hz–0.40 Hz), which reflects parasympathetic activity. LF refers to the low-frequency range of power (0.04 Hz–0.15 Hz), which represents sympathetic and parasympathetic activity; LF/HF refers to the ratio of low and high-frequency power ratio in %, which represents the autonomic nerve.

The wavelet transform algorithm is selected to denoise the ECG signal in this paper. The fundamental principle of wavelet denoising is an algorithm based on the multiresolution analysis of wavelet transform. With the basic idea that the wavelet decomposition coefficients of noise and signal in different frequency bands have different intensity distribution, the wavelet coefficients corresponding to the noise in each frequency band are removed to retain the wavelet decomposition coefficients of the original signal.

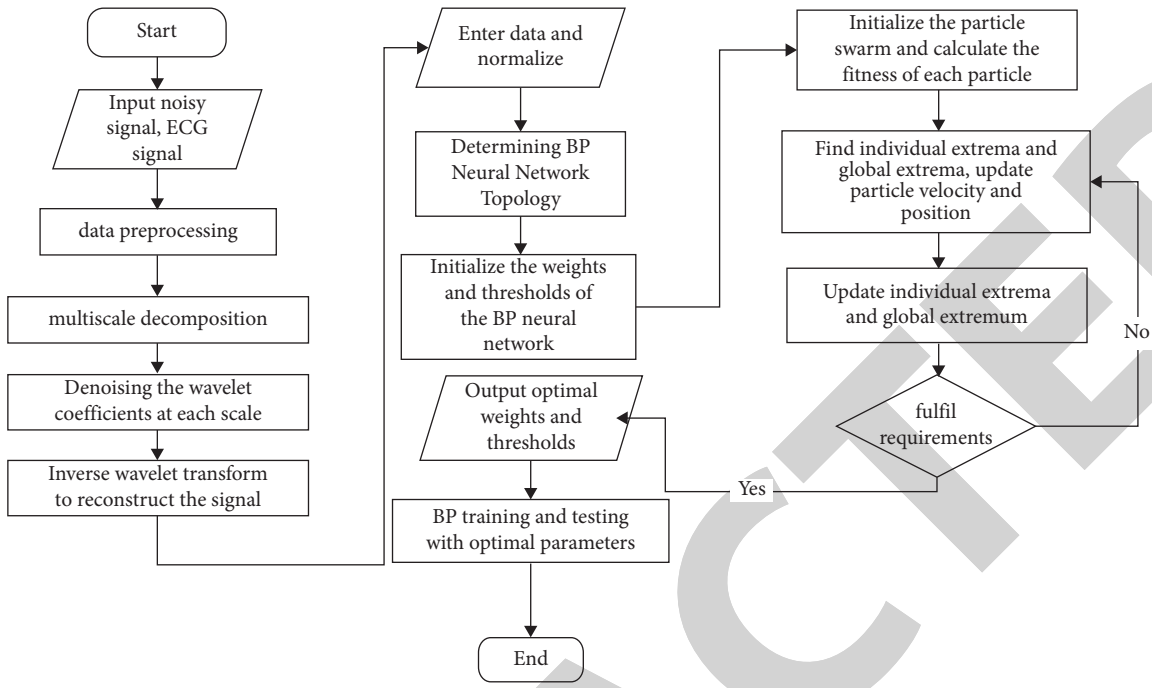

Figure 1: Flow chart of PSO-BP neural network-based prediction model.

Then, it performed wavelet reconstruction of the processed coefficients to obtain the denoised signal [12, 13]. Its advantage is that the recognition rate of the signal after wavelet transform denoising is higher compared with other denoising algorithms, and it is especially effective in denoising time-varying signals and abrupt signals. The wavelet basis in the paper selects the bior wavelet basis to obtain the corresponding detail coefficients and approximation coefficients after the 8-layer wavelet decomposition of the one-dimensional ECG signal (the wavelet type of the wavedec function under MATLAB is bior2.6). Then, the detail coefficients of 1 and 2 layers contain most of the high-frequency noise, and the approximation coefficients of 8 layers include the baseline drift according to the wavelet principle. A denoising signal with no baseline drift is obtained based on this by setting the detail coefficients of layers 1 and 2 and the approximation coefficients of layer 8 after the corresponding wavelet reconstruction [14].

In the case of multiresolution, the scale function and the wavelet function together construct the decomposition of the signal. The scale function can be constructed by a low-pass filter, while the wavelet function is implemented by a high-pass filter. With such a filter bank, the framework of the decomposition is formed. It is possible to use the scale function of the low-pass filter as the parent function of the wavelet function and the scale function of the next level. The scale function characterizes the low-frequency features of the signal. It is the wavelet function that really approximates the high-frequency basis. The wavelet function can be constructed using the scale function [15, 16]. The wavelet transform basic process is as follows: 1. select the appropriate wavelet function and scaling function to inversely calculate the coefficients a and d from the existing signal; 2. perform the corresponding processing on the coefficients; 3. reconstruct the signal from the processed coefficients, as shown in Figure 2.

2.3. PSO-BP Neural Network Model

2.3.1. The Basic Principle of BP Neural Network. The BP neural network algorithm is a multilayer feed-forward supervised artificial neural network. Each node represents a neuron. The neurons in the previous and the following layers are connected by corresponding weights [17]. For the BP neural network, the learning training is mainly split into a forward transmission of the signal and backward transmission of the error. The forward transmission of the signal is to pass the input signal to the implicit layer and the output layer to obtain the predicted output. The error signal is then obtained from the predicted and expected outputs. The process of error backward transmission is to feed the error signal back to the previous neural network. Then, the corresponding weights and thresholds are adjusted according to the magnitude of the errors. In general, an error gradient descent method is followed for this process, and the BP neural network first trains the top layer of the network. Its weights and thresholds are fixed after training, and then, the output of its hidden unit is used as the input vector for the next layer of the network to continue training. After all the networks are trained, the weights and thresholds are adjusted by the backward transmission algorithm in a continuous iterative cycle until the error signals of the predicted and desired outputs meet the target requirements and are then terminated [18–20].

It is assumed that the neuron in the input layer of the BP neural network is $x_1, x_2, \ldots, x_m$, and the output of the j th

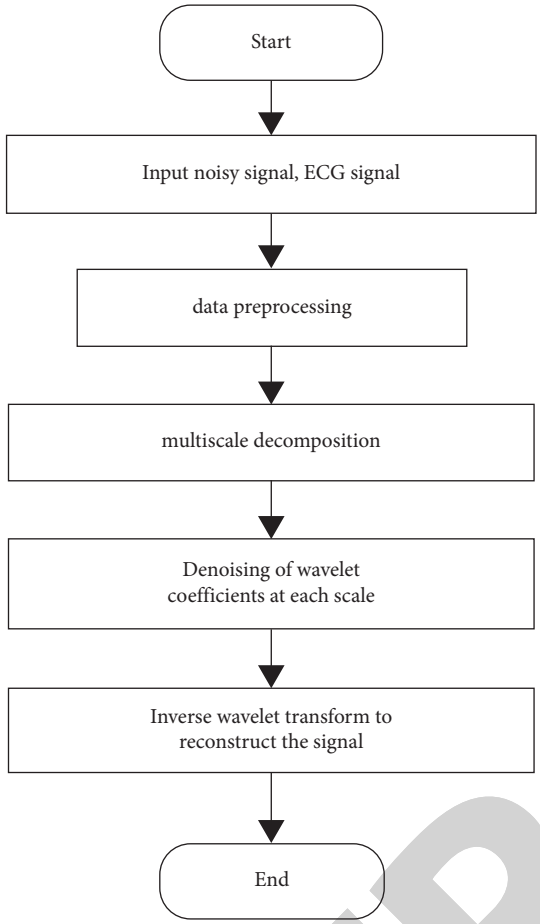

Figure 2: Signal denoising based on wavelet transform algorithm.

neuron after being stimulated by the last neuron from 1 to m is represented as $w_{j1}, w_{j2}, \ldots, w_{jm}$. As shown in (1), S_j is the net input value of the j th neuron.

BP neural network algorithm is a multilayer feed-forward supervised artificial neural network, which continuously adjusts the connection weight and threshold between each neuron through the training process of forward propagation of input signal and back propagation of error signal, as shown in Figure 3. Suppose that the input of neurons from 1 to n in BP neural network is $x_1, x_2, \ldots, x_m$, and let the output of the jth neuron after being stimulated by the last neuron from 1 to n be expressed as $w_{j1}, w_{j2}, \ldots, w_{jm}$. As shown in (6), it is the net input value of the j th neuron:

$$\begin{aligned} S_j &= \sum_{i=1}^{m} w_{ji} * x_i + b_j \\ &= W_j X + b_j. \end{aligned} \tag{6}$$

Among them, $X = [x_1, x_2, \ldots, x_m]^T$, Wj = $[w_{j1}, w_{j2}, \ldots, w_{jm}]$,

If $x_0 = 1, w_{j0} = b_j$ is set, it is included in the input signal, and the input offset bj becomes a weight element, and then, $X = [x_1, x_2, \ldots, x_m]^T$ and Wj = $[w_{j1}, w_{j2}, \ldots, w_{jm}]$. As shown in (7), it is a simple expression of the output after the action of the excitation function:

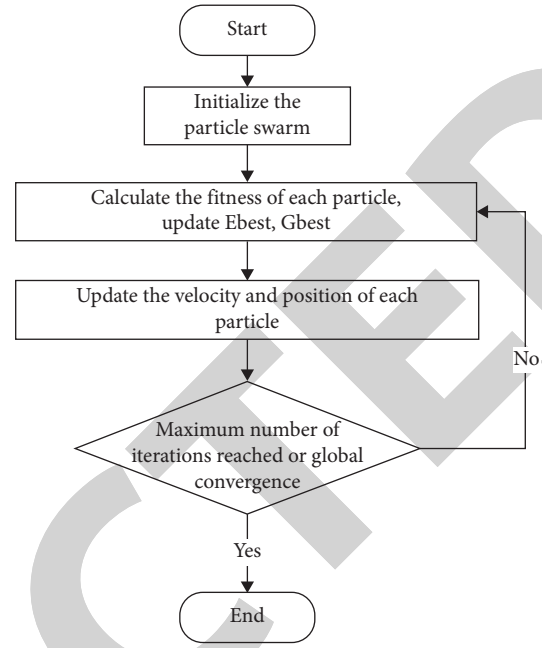

Figure 3: PSO algorithm flow chart.

$$\begin{aligned} O_i &= f\left(S_j\right) \\ &= f\left(\sum_{i=1}^{n} w_{\mathrm{ji}} * x_i\right) \\ &= F\left(W_j * X\right), \end{aligned} \tag{7}$$

$$\mathrm{Net}_i = \sum_{j=1}^{M} w_{ji} * x_i + \theta_i, \tag{8}$$

θ_i is the bias vector of the hidden layer, that is, $\theta = (\theta_1, \theta_2, \ldots, \theta_q)^T$. Where $\varphi(x)$ is the transfer function of the hidden layer. The input and output expressions of the output layer are shown in the following formulas:

$$\mathrm{Net}_k = \sum_{i=1}^{M} w_{ki} * O_i + \alpha_k, \tag{9}$$

$$T_k = \gamma\left(\mathrm{Net}_k\right), \tag{10}$$

where α_{k} is the offset vector of the input layer, namely $\alpha = (\alpha_1, \alpha_2, \ldots, \alpha_L)^T$. Where $T = (T_1, T_2, \ldots, T_L)$ is the output vector. The excitation function is shown in the following formula:

$$f = \frac{1}{1 + e^{-x}}. \tag{11}$$

After the BP neural network obtains the output value, it compares with the ideal output value to obtain the prediction error e_k [21], as shown in the following formula:

$$e_k = Y_k - T_K, \tag{12}$$

where Y_k is the ideal output value.

A selection of the number of neurons in the hidden layer is made according to the following formula where m is the number of neurons in the input layer and n is the number of neurons in the output layer.

$$P = \frac{1}{2}(2m + n). \tag{13}$$

2.3.2. Fundamentals of PSO Algorithm. The PSO algorithm treats the location or food of individuals in a flock as the solution to an optimization problem. By taking advantage of the interaction of information between individuals in the population and the optimal individual and between individuals, the particles in the population as a whole are guided to converge toward the optimal individual while retaining information about the diversity of individuals. The optimal solution is found gradually by continuous updating. PSO is a metaheuristic algorithm because it makes few or no assumptions about the problem being optimized and is able to search a very large candidate solution space.

The PSO algorithm is initialized as a random population of particles, and then, the optimal solution is found through multiple iterations. Particles update themselves during each iteration by the optimal solution found by themselves and the optimal solution found so far by the whole population. It is also possible to update itself using the extremes of the particle's own neighbors. A smaller result obtained by bringing the position of the particle into the fitness function is a better result [22–24]. Assume that in the target search space, the total size of the particle population is N, the current number of iterations is t, the position of the number of $i\,(i = 1, 2, \ldots, N)$ particle in the population is $P_i(t) = [P_{i1}(t), P_{i2}(t), \ldots, P_{\text{in}}(t)]$, the velocity of the ith particle is $V_i(t) = [V_{i1}(t), V_{i2}(t), \ldots, V_{\text{in}}(t)]$, the current optimal position searched for by the ith particle is $E_{\text{best}}(t) = [e_{i1}(t), e_{i2}(t), \ldots, e_{\text{in}}(t)]$, and the current optimal position searched for by all particles in the entire population in the nth dimension is $G_{\text{best}} = [g_1(t), g_2(t), \ldots g_n(t)]$. The formula for updating the velocity and position of a particle using the particle optimal value and the global optimal value is shown as follows:

$$\begin{aligned} V_{in}(t+1) &= W * V_{in}(t) + C_1 R_1 \left(E_{\text{best}-in}(\pi) - P_{in}(t)\right) + C_2 R_2 \left(G_{\text{best}-n}(t) - P_{in}(t)\right), \\ P_{in}(t+1) &= P_{in}(t) + V_{in}(t) + 1, \end{aligned} \tag{14}$$

where C_1, C_2 are the acceleration constant. It can also be referred to as the learning rate, which is used to regulate the maximum step of learning. W is the inertia constant, which is nonnegative and is used to regulate the degree of influence of the last speed on the current speed. R_1, R_2 are a random number in the range of [0, 1], which is used to increase the random searchability. The flow chart of the PSO algorithm is shown as follows.

2.3.3. PSO-BP Neural Network Prediction Model. The procedure of the algorithm for prediction of driver reaction time using PSO optimized BP neural network is as follows:

(1) *Data Preprocessing*. The sample data are read, and the data set and test set are generated.

(2) *Model Parameters Setting*. According to the characteristics of the input data, set the number of neurons in the hidden layer of the BP neural network model, the maximum number of iterations, and the termination condition.

(3) The connection weights and thresholds of the BP neural network are optimized by the particle swarm algorithm.

(4) Establish the PSO-BP neural network prediction model. A testing set is used to test the trained neural network and output the prediction results.

The number of neurons in the input layer of the BP neural network is 6, and the number of neurons in the output layer is 1. It was found that when the number of nodes in the hidden layer of the network is set to 7, the performance of the network is better in all aspects, and the model structure of this paper is designed as 6-7-1. The other parameters of the BP neural network are set as follows: the transfer function of the hidden layer is tansig, the output layer transfer function is tansig, the maximum number of iterations is 1000, and the global minimum error is 0.005. The formula of the adaptability function in this paper is shown as follows:

$$\text{fitness} = \text{sum}\left(\text{abs}\left(Y_k - T_K\right)\right), \tag{15}$$

where Y_k is the predicted output of the BP neural network, and T_K is the true value of the sample output.

3. Experimental Design and Data Processing

3.1. Experimental Equipment and Experiment Design. A simulated automated vehicle platform was built using PRESCAN driving simulator, and a single channel screen is used for the front view system. The driving simulator records test data from the vehicle and surrounding objects in real time with 20 Hz, such as vehicle speed, acceleration, and steering angle. The driving simulator includes an adjustable seat, wheel and pedal supports, LOGITECH Driving Force GT® steering wheel with force feedback, a throttle pedal, and a brake pedal. The driving scenario was presented on the monitors. Besides, other types of equipment are tablet PC for playing SuRT tasks, audio equipment for playing n-back tasks, and computer for collecting data. The driving simulator and physiograph acquisition platform are shown in Figure 4.

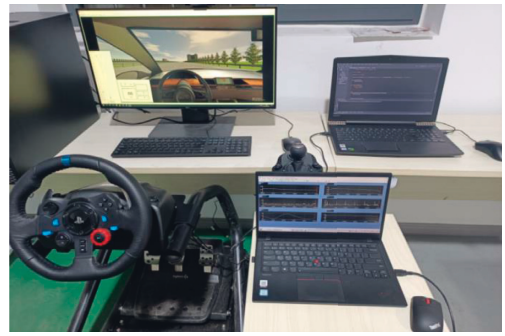

Figure 4: Driving simulator and physiometer acquisition platform.

3.1.1. Experimenting with Triggering Events and Nondriving Tasks. This paper has four typical hazardous conditions based on the SOTIF triggering event. In the first triggering event, the system failure is based on the failure of the sensing system, such as the lane line ahead of the highway is missing or blurred so that the lane keeping system (LKA) cannot detect the lane line, resulting in the system failure triggering SOTIF. The system is designed to exceed the operational design domain (ODD) in the second triggering event, where a pedestrian suddenly appears on the highway and a sensor in front detects this pedestrian. In the third triggering event, a warning is issued when an object (faulty car) appears ahead on the highway that cannot be recognized due to sensor performance limitations. In the fourth triggering event, the target car cuts in front of the vehicle at a certain speed, and the sensing system does not recognize it and issues a warning. A sample simulation scenario is shown in Figures 5 and 6. In the triggering scenario, the selected road is a two-way 5-lane highway with a total length of 30 Km. The autonomous emergency braking (AEB) and LKA modules are added to the autonomous driving system. After debugging, visual and auditory warning signals were added to the expected functional triggering scenario based on SIMULINK. The overall test time for the driver was set to 70 minutes, and four trigger events were set as a set of tests because of the difference between the simulation time and the actual time. The interval between each stimulus signal was 15 seconds, making 70 trials. Therefore, a total of 280 reaction times were collected for each driver. As a result, 2800 sets of reaction time data were collected for a total of 10 drivers. There were 302 warning stimuli designed for this experiment. The data were first screened because drivers had mistakenly triggered the record time button, did not trigger the record time button, and continuously triggered the record time button. The average number of reaction times recorded per driver was 286.8.

Furthermore, the nondriving tasks that affect the driver's workload are introduced in this paper in order to measure the factors influencing the driver's reaction time. The designed nondriving tasks include two types of auditory and visual tasks. The auditory nondriving task is n-back with monitoring subtask, and the visual nondriving task is arrow vision with SuRT (surrogate reference task) subtask. The SuRT visual nondriving task is frequently used in takeover and reaction time tests [25, 26]. It is required that the driver's hand holds the steering wheel, keeps the eyes looking ahead of the road, and keeps the feet free from any manipulation to satisfy the driver's requirements for L3 level autonomous driving takeover. A 2-back test was selected as the auditory distraction and workload increase test task in this paper. The driver will be given auditory stimuli signal to play through this task, and the driver will respond by pressing the *L* letter. Each stimulus signal will consist of a single letter, and it will be played randomly. The interval between each stimulus signal will be 3.2 seconds. The driver will be asked to press the *L* key based on the first two played letters. For example, the system reports ABACDFD in sequence. When the system reports AB, the driver does not press *L*; when it reports the third letter A and then press *L*; when it reports CDF, the driver responds; when it reports the seventh letter *D*, the driver presses *L*, and so on. There were 1052-second trials designed to meet the test requirements. The arrow visual subtask was selected for a $4 * 4$ matrix, as shown in Figure 7. The driver was asked to identify the upward arrow and make a mark.

The combination of visual and auditory alerts is used as the stimulus signal in this paper since the inclusion of nondriving tasks contains both visual and auditory tasks. A button on the steering wheel is used to record the driver reaction time when the driver observes the visual warning signal or hears a beeping sound. Details of the design of the nondriving tasks and trigger events are shown in Table 1. It was designed using the Latin square design method for the overall experimental sequence.

3.1.2. Test Procedure. Upon arrival at the trial room, the subjects are first required to sign an informed consent form and fill out a questionnaire. Subsequently, they were given a briefing by the test assistant on the test precautions and were given an explanation of the test tasks in conjunction with the simulator and other equipment. The subjects then go through exercises to familiarize themselves with the driving simulator and nondriving tasks and put on the physiological equipment. The subjects started the formal trial after the exercises.

3.2. Data Preprocessing and Data Analysis

3.2.1. Driver Reaction Time Data Analysis. Driver reaction time is a critical element of accident reconstruction technology and an essential aspect of driver risk assessment

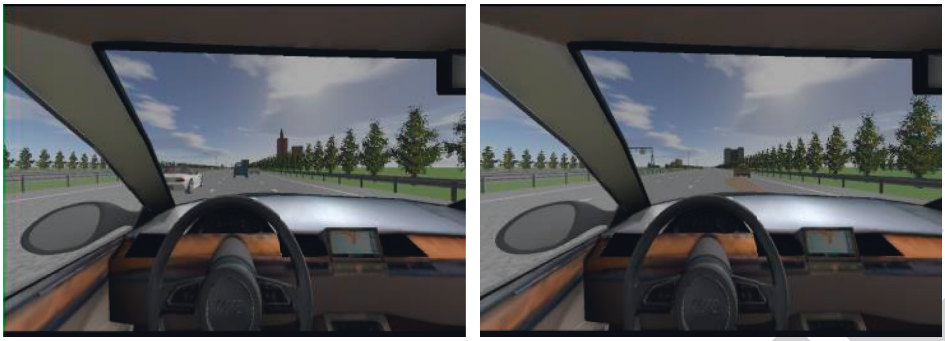

Figure 5: Highway experiment simulation scenario.

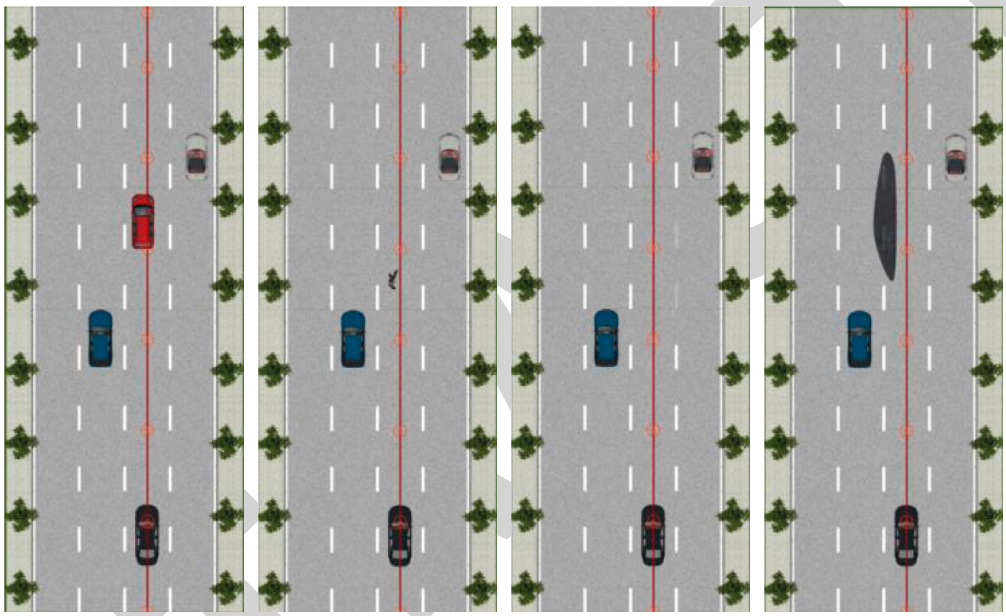

Figure 6: Four trigger events designed based on the safety of the intended functionality.

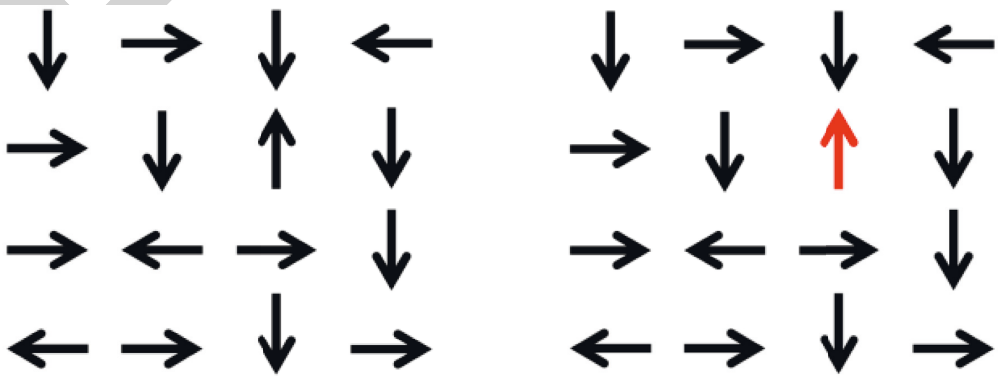

Figure 7: Nondriving tasks—arrow visual subtasks.

because the length of driver reaction time directly affects the crash time when the driver takes avoidance measures and affects the design of takeover time in various scenarios in autonomous driving. These factors are considered in the driver reaction time test in this paper, such as the driver mistakenly triggering the record time button, not triggering the record time button, and continuously triggering the record time button. Thus, the abnormal driver reaction time data need to be processed. 1422 sets of valid driver reaction time data were obtained after eliminating the abnormal data,

Table 1: Human-machine codriving test grouping design.

Test	Risky scenario work conditions	Nondriving tasks	Autonomous driving levels	Warning method	How to record reaction time
1	Static obstacle in front	2-back	Look at the road	Visual + auditory	Steering wheel buttons
2	Static obstacle in front	Monitoring	Look at the road	Visual + auditory	Steering wheel buttons
3	Pedestrian in front	2-back	Look at the road	Visual + auditory	Steering wheel buttons
4	Pedestrian in front	Monitoring	Look at the road	Visual + auditory	Steering wheel buttons
5	Worn lane lines	2-back	Look at the road	Visual + auditory	Steering wheel buttons
6	Worn lane lines	Monitoring	Look at the road	Visual + auditory	Steering wheel buttons
7	Front cut-in (speeding)	2-back	Look at the road	Visual + auditory	Steering wheel buttons
8	Front cut-in (overspeeding)	Monitor	Look at the road	Visual + auditory	Steering wheel buttons
9	Static obstacle ahead	SuRT	No look at the road	Visual + auditory	Steering wheel buttons
10	Static obstacle ahead	Arrow vision	No look at the road	Visual + auditory	Steering wheel buttons
11	Pedestrian ahead	SuRT	No look at the road	Visual + auditory	Steering wheel buttons
12	Pedestrian ahead	Arrow vision	No look at the road	Visual + auditory	Steering wheel buttons
13	Worn lane lines	SuRT	No look at the road	Visual + auditory	Steering wheel buttons
14	Worn lane lines	Arrow vision	No look at the road	Visual + auditory	Steering wheel buttons
15	Front cut-in (speeding)	SuRT	No look at the road	Visual + auditory	Steering wheel buttons
16	Front cut-in (speeding)	Arrow vision	No look at the road	Visual + auditory	Steering wheel buttons

as shown in Figure 8. The mean value of reaction time, standard deviation, and the overall data obey normal distribution.

3.2.2. Driver Physiological Data Processing and Analysis. In this paper, the sampling rate of each driver's ECG signal is 256 Hz, the signal duration is 6300 seconds, and the total length of the signal, or the total number of data sampling points, is 1612800. In this paper, each driver's ECG signal has a sampling rate of 256 Hz, a signal duration of 6300 seconds, and the total length of the signal, which is the total number of data sampling points, is 1612800. In order to calculate each segment of HRV, the original ECG data were segmented. A wavelet transform algorithm was used to preprocess the data, and the signal pairs before and after the original signal denoising are shown in Figure 9. It can be seen from the before-and-after analysis that the corresponding detail coefficients and approximation coefficients are obtained after the 8-layer wavelet decomposition of the one-dimensional ECG signal based on the bior wavelet basis. The noise signals, such as industrial frequency interference and baseline drift, are eliminated. Moreover, it has achieved an excellent denoising effect by maintaining the waveform and detailed information of the original ECG signal to a large extent.

It is a prerequisite for ECG signal analysis to obtain HRV signals. The intermittent spectrum method is used to obtain the HRV signal from the ECG signal in this paper. The denoised ECG data are first processed, and then, the R-wave of the ECG signal is located using the pantompkins_qrs algorithm, as shown in Figure 10. After extracting the R-wave using the interval spectrum method, the RR intervals were obtained by subtracting the times of R-wave appearance one by one. With the algorithm in this paper, the RR interval value (in seconds) is calculated by the RR interval. Finally, it extracts the time-frequency characteristic parameters in the RR interval of the HRV signal.

We firstly normalize the extracted feature parameters for the purpose of unifying the magnitudes and improving the speed and accuracy of model training. Then, the HRV feature parameter vector is obtained by writing a program in Matlab to decompose and reconstruct the wavelet packet of the noise-reduced ECG signal. The formula $y = (x - \min)/(\max - \min)$ is used to normalize it to an interval, and the normalized training sample data are used to find the abnormal data with box plots, as shown in Figure 11(a). Exception values are processed by the mean correction method (i.e., correcting the outlier with the mean of the two observations before and after). The processed data are shown in Figure 11(b). They are taken as the training and testing sample data of the PSO-BP neural network model.

The correlation between ECG signal and driver reaction time can be obtained according to Pearson correlation analysis, and the characteristic input parameters of the PSO-BP neural network model are selected. The analysis results of each characteristic parameter are shown in Table 2. Based on the correlation analysis results, a total of six time-frequency domain feature parameters are selected as the input parameters of the PSO-BP neural network algorithm, including four time-domain indicators, NNVGR, SDNN, RMSSD, and SDSD, and two frequency domain indicators, TP and HF.

4. Analysis of Results

There were 302 warning stimuli signals designed for this test. The data were first screened because drivers had mistakenly triggered the record time button, did not trigger the record time button, continuously triggered the record time button, etc. On average, the reaction time recorded per driver was 286.8 times. The intermittent spectrum method was used to obtain the HRV signal from the ECG signal. After the denoised ECG data were processed to calculate the RR interval values, the time-domain and frequency-domain feature parameters were extracted. The extracted feature parameters were brought into the PSO-BP neural network for training. In this experiment, the number of neurons in the input layer is 6, and the number in the output layer is 1. It is found that the network's performance is better when the number of nodes in the hidden layer is set to 7.

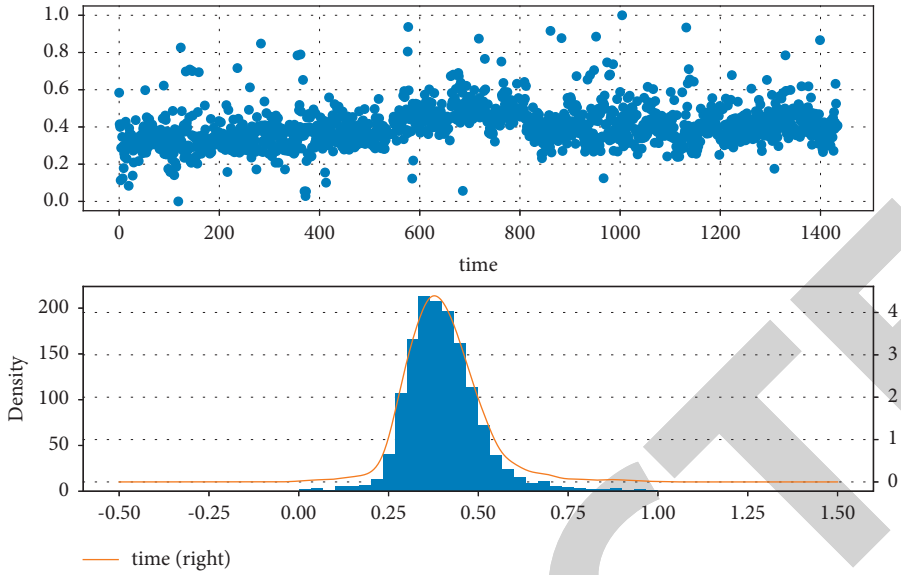

Figure 8: Driver reaction time data distribution.

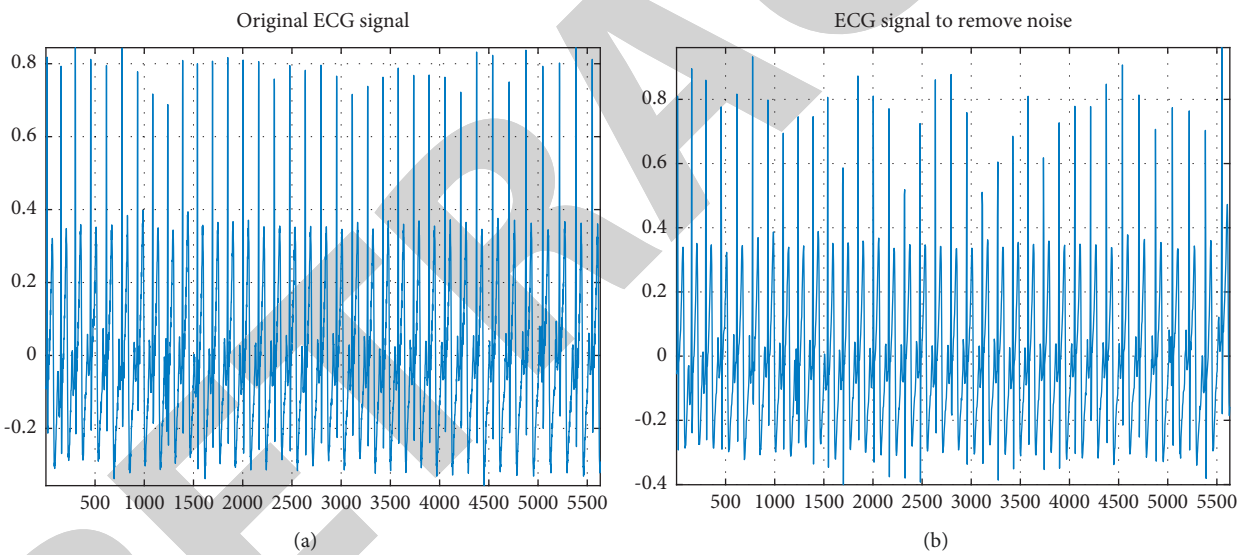

Figure 9: Comparison of ECG original signal and denoised signal.

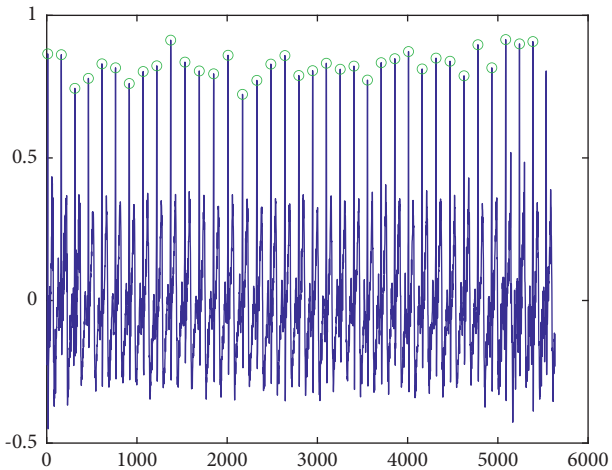

Figure 10: R-wave diagram of the localized ECG signal.

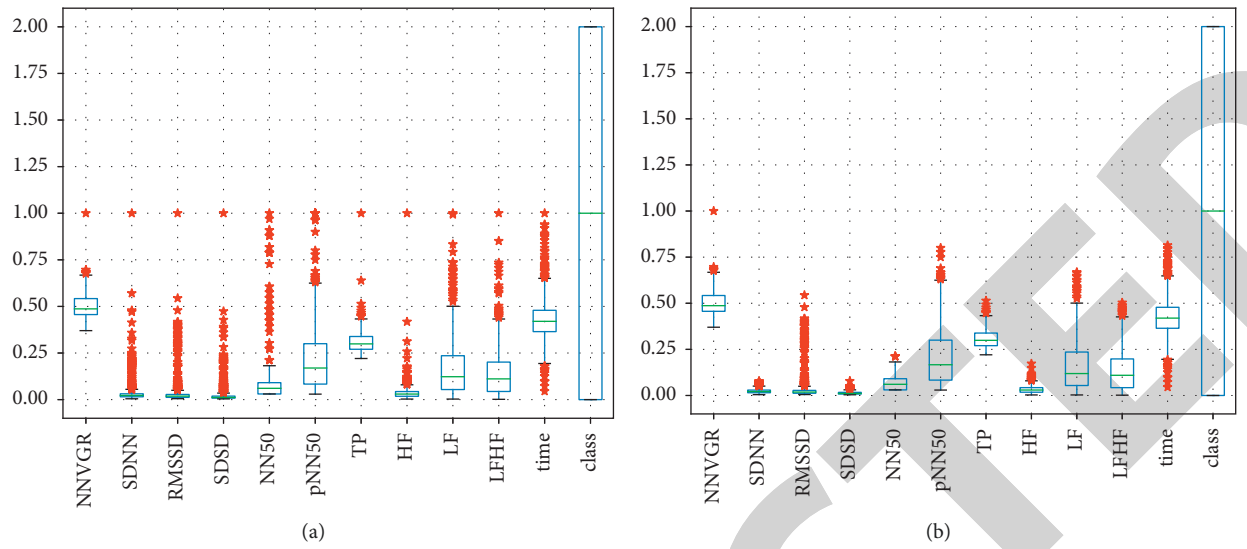

Figure 11: Feature parameter outlier detection and processing.

Table 2: Correlation analysis between reaction time and HRV characteristic parameters.

	ECG signal		*R* value	*P* value
Driver reaction time	Time domain indicators	NNVGR	0.2409420	2.12319e-20
		SDNN	−0.1160284	1.05112e-05
		RMSSD	−0.1265519	1.51584e-06
		SDSD	−0.095468	0.000292
		NN50	−0.0770747	0.003483
		pNN50	0.0827392	0.001707
	Frequency domain indicators	TP	0.1440193	4.2655722e-08
		HF	−0.11478483	1.307569e-05
		LF	0.088763	5.623940e-13
		LF/HF	−0.072569	0.0059548

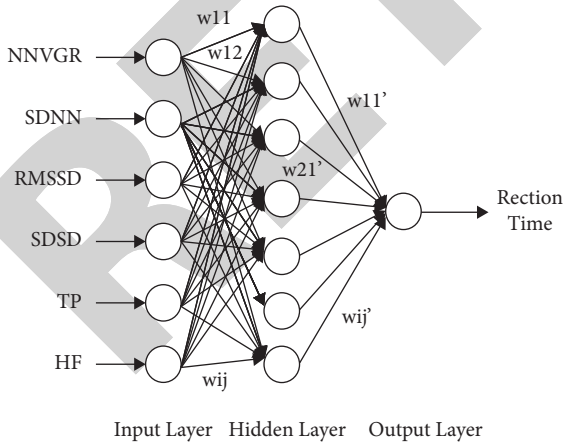

Figure 12: Actual model of PSO-BP neural network.

Consequently, the structure of the BP neural network model was designed as 6-7-1, and the extracted six feature parameters were brought into the PSO-BP neural network model. The specific design of the input layer, hidden layer, and output layer is shown in Figure 12. In the case of the BP neural network, the other parameters are set as follows: the implicit layer transfer function is tansig, the output layer transfer function is tansig, the maximum number of iterations is 1000, and the global minimum error is 0.005. The connection weights and thresholds of the 57 neural networks updated by the PSO algorithm are shown in Figure 13. The optimized weights and thresholds are substituted into the BP neural network for training using the particle swarm algorithm.

Data from a sample of 10 drivers are used as training set and testing set in this paper. Then, the processed data are brought into the PSO-BP neural network prediction algorithm proposed in this paper for training and testing. RMSE is used as the evaluation index and is a standard measure of the difference between the model's predicted value and the actual value of the driver's reaction time. It is shown as follows:

$$\mathrm{RMSE} = \sqrt{\frac{1}{n}\sum_{i=1}^{n}\left(O_{\mathrm{predict}} - O_{\mathrm{real}}\right)^2}. \tag{16}$$

The value of O_predict is the predicted reaction time of the PSO-BP neural network model, O_real is the actual

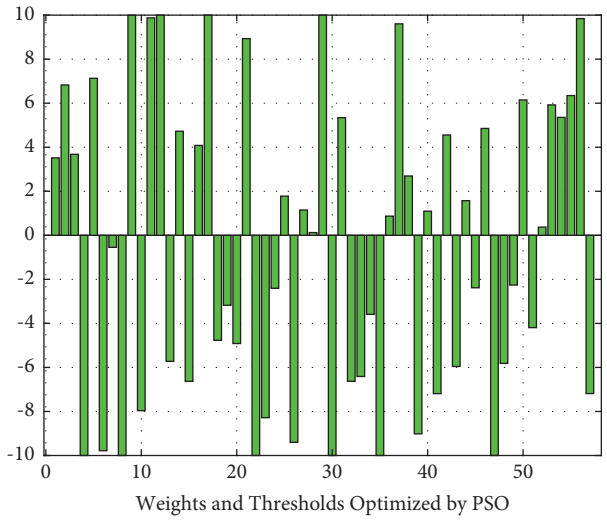

Figure 13: PSO algorithm to optimize the weights and thresholds of the BP neural network.

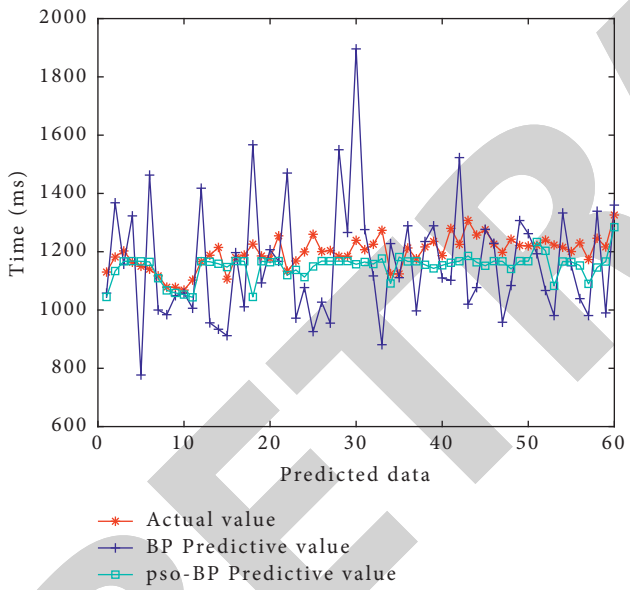

Figure 14: Comparison of PSO-BP neural network-based and BP neural network algorithms.

driver reaction time, and N is the sample size. It is based on the PSO-BP neural network algorithm is 230.2829 ms, and that based on BP neural network algorithm is 233.2669 ms. It can be seen that the accuracy of the PSO-BP neural network algorithm proposed in this paper is better than the BP neural network algorithm. Figure 14 gives the comparison between the predicted data and the actual data of driver reaction time by BP neural network and PSO-BP neural network. Obviously, the predicted values based on PSO-BP neural network algorithm are closer to the real values as shown in the figure. Meanwhile, the absolute value of the error obtained by calculating the error between the predicted value and the real value is shown in Figure 15. As shown in the results, the prediction accuracy of the

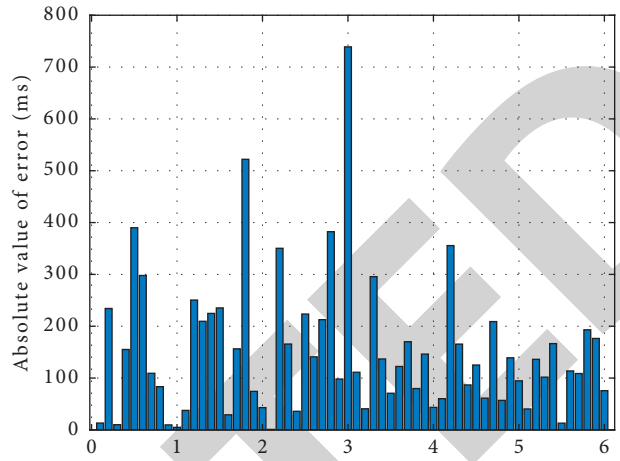

Figure 15: Absolute value of error based on PSO-BP neural network.

PSO-BP neural network algorithm based on the prediction of driver reaction time is better than that of the BP neural network. The model proposed in this paper achieves the expected objectives.

5. Conclusion

A simulated automated vehicle platform was built using PRESCAN driving simulator, and four typical hazardous conditions are designed based on the SOTIF trigger scenario. Two types of alarm signal, visual and auditory, are added to the scenarios. An approach to predict the driver's reaction time using raw physiological data is proposed. We started the study with driver reaction time since the takeover time in the SOTIF-degraded mode includes the driver reaction time and an approach based on PSO-BP neural network is proposed in this paper. It is specifically designed as a simulated automated vehicle platform test to analyze the relationship between driver ECG signal feature indicators and driver reaction time under nondriving tasks. The data were used as the input signal of the PSO-BP neural network after denoise by the wavelet transform algorithm. Simultaneously, Pearson correlation analysis was used to select the ten feature parameters of the input. From the analysis, six time-frequency domain feature parameters were extracted as data input to the model. The weights and thresholds of the BP neural network are optimized based on the PSO algorithm; thus, a PSO-BP neural network model is established. Finally, a comparison of the prediction results obtained from the PSO-BP neural network model with the actual data is performed. It is demonstrated that the error obtained by the proposed algorithm in this paper is much less and smaller. The reasonableness and effectiveness of the model are verified, and the accurate prediction of the driver's reaction time under the SOTIF trigger scenario is achieved. Meanwhile, an essential theoretical basis for designing and developing a driver takeover time prediction system in SOTIF fail-degraded mode is provided for the driver takeover time evaluation of control switching in *L*3+ autonomous driving systems.

Data Availability

Authors can also make data available on request through a data access committee, institutional review board, or the authors themselves.

Conflicts of Interest

The authors declare that they have no conflicts of interest.

Acknowledgments

This paper was supported by the Natural Science Basic Research Plan in Shanxi Province of China (2018JM6089), the National Natural Science Foundation of China (52172388), and the Tianjin Postgraduate Research and Innovation Project Funding (2021YJSO2B14).

References

[1] X. Ma and I. Andréasson, "Estimation of driver reaction time from car-following data," *Transportation Research Record: Journal of the Transportation Research Board*, vol. 1965, no. 1, pp. 130–141, 2006.

[2] R. S. Jurecki, "Driver's reaction time under emergency braking a car-research in a driving simulator," *Eksploatacja i Niezawodność*, vol. 14, no. 4, pp. 295–301, 2012.

[3] P. DroździelDroździel and R. TarkowskiRybickaWrona, "Drivers 'reaction time research in the conditions in the real traffic," *Open Engineering*, vol. 10, no. 1, pp. 35–47, 2020.

[4] G. Johansson and K. Rumar, "Drivers' brake reaction times," *Human Factors: The Journal of the Human Factors and Ergonomics Society*, vol. 13, no. 1, pp. 23–27, 1971.

[5] U. Durrani and D. Shah, "Predicting driver reaction time and deceleration: comparison of perception-reaction thresholds and evidence accumulation framework," *Accident Analysis & Prevention*, vol. 149, Article ID 105889, 2021.

[6] R. Jurecki, "Driver response time in different traffic situations for using in accident analysis," *Zeszyty Naukowe Instytutu Pojazdów/Politechnika Warszawska*, vol. 2/106, pp. 45–60, 2016.

[7] M. Elhenawy, I. El-Shawarby, and H. Rakha, *Modeling the Perception Reaction Time and Deceleration Level for Different Surface Conditions Using Machine Learning Techniques, Advances in Intelligent Systems and Computing*, Springer, Cham, pp. 131–142, 2017.

[8] M. Poliak and E. SvabovaBenusDemirci, "Driver response time and age impact on the reaction time of drivers: a driving simulator study among professional-truck drivers," *Mathematics*, vol. 10, no. 9, p. 1489, 2022.

[9] Y. Nowosielski, B. Leitner, T. Rauchegger et al., "Bilateral cataract surgery improves neurologic brake reaction time and stopping distance in elderly drivers," *Acta Ophthalmologica*, vol. 99, no. 7, Article ID e1017, 2021.

[10] N. Arbabzadeh, M. Jafari, M. Jalayer, S. Jiang, and M. Kharbeche, "A hybrid approach for identifying factors affecting driver reaction time using naturalistic driving data," *Transportation Research Part C: Emerging Technologies*, vol. 100, pp. 107–124, 2019.

[11] R. S. Jurecki and T. Lech Stańczyk, "Analyzing driver response times for pedestrian intrusions in crash-imminent situations," in *Proceedings of the 2018 XI International Science-Technical Conference Automotive Safety*, April 2018.

[12] D. M. Chandrappa and S. M. Kiran, *Plant Disease Identification Using Discrete Wavelet Transforms and SVM*, 2021.

[13] I. Moumene and N. Ouelaa, "Gears and bearings combined faults detection using optimized wavelet packet transform and pattern recognition neural networks," *International Journal of Advanced Manufacturing Technology*, vol. 120, no. 7-8, pp. 4335–4354, 2022.

[14] X. H. Wang, R. S. Istepanian, and Y. H. Song, "Microarray image enhancement by denoising using stationary wavelet transform," *IEEE Transactions on NanoBioscience*, vol. 2, no. 4, pp. 184–189, 2003.

[15] P. Rajeswari, "Denoising X-Ray Image Using Discrete Wavelet Transform and Thresholding," *Futuristic Communication and Network Technologies*, Springer, Singapore, 2022.

[16] D. WuWu and S. WangWu, "A hybrid method based on extreme learning machine and wavelet transform denoising for stock prediction," *Entropy*, vol. 23, no. 4, p. 440, 2021.

[17] Y. S. Pei, "Evaluation of urban landscape planning and design based on BP neural network model," *Journal of Inner Mongolia Normal University (Natural Science Edition)*, 2018.

[18] B. Zhang and H. Jin, "Production forecast analysis of BP neural network based on Yimin lignite supercritical water gasification experiment results," *Energy*, vol. 246, Article ID 123306, 2022.

[19] Q. S. Hong and T. Chen, "The MRO purchasing forecast of chemical equipment based on BP neural network," *Logistics Engineering and Management*, 2016.

[20] H. W. Chen and Y. Meng, "Prediction of solid circulation rate in an internal circulating fluidized bed with draft tube based on gentic algorithm BP neural network," *Boiler Technology*, vol. 2013, 2013.

[21] A. Sl and B. Zf, "Evaluation of urban green space landscape planning scheme based on PSO-BP neural network model," *Alexandria Engineering Journal*, vol. 61, pp. 7141–7153, 2022.

[22] J. Cao and J. LuWangWang, "A loan default discrimination model using cost-sensitive support vector machine improved by PSO," *Information Technology and Management*, vol. 14, no. 3, pp. 193–204, 2013.

[23] R. K. Yadav and Anubhav, "PSO-GA based hybrid with Adam Optimization for ANN training with application in Medical Diagnosis," *Cognitive Systems Research*, vol. 64, pp. 191–199, 2020.

[24] Na. Li and M. Li, "Forecast of chemical export trade based on PSO-BP neural network model," *Journal of Mathematics*, vol. 2022, Article ID 1487746, 10 pages, 2022.

[25] J. Wan and C. Wu, "The effects of lead time of take-over request and nondriving tasks on taking-over control of automated vehicles," *IEEE Transactions on Human-Machine Systems*, vol. 48, no. 6, pp. 582–591, 2018.

[26] H. Clark and J. Feng, "Age differences in the takeover of vehicle control and engagement in non-driving-related activities in simulated driving with conditional automation," *Accident Analysis & Prevention*, vol. 106, pp. 468–479, 2017.